ACS APPLIED MATERIALS & INTERFACES

Research Article

Cite This: ACS Appl. Mater. Interfaces 2018, 10, 39512−39523

www.acsami.org

Nanoroughness, Surface Chemistry, and Drug Delivery Control by Atmospheric Plasma Jet on Implantable Devices

Alessandro Patelli,[*,†] Federico Mussano,[‡] Paola Brun,[§] Tullio Genova,[‡,∥] Emmanuele Ambrosi,[⊥] Niccoló Michieli,[†] Giovanni Mattei,[†] Paolo Scopece,[#] and Lorenzo Moroni[¶]

[†]Department Physics and Astronomy, Padova University, via Marzolo 8, 35131 Padova, Italy

[‡]CIR Dental School, Department Surgical Sciences, Torino University, 10126 Torino, Italy

[§]Department Molecular Medicine, Unit of Microbiology, Padova University, 35121 Padova, Italy

[∥]Department Life Sciences and Systems Biology, Torino University, 10124 Torino, Italy

[⊥]Department Molecular Sciences and Nanosystems, Venezia University, 30172 Venezia, Italy

[#]Nadir srl, 30172 Venezia, Italy

[¶]MERLN—Institute for Technology-Inspired Regenerative Medicine, Maastricht University, 6229 ER Maastricht, The Netherlands

Supporting Information

ABSTRACT: Implantable devices need specific tailored surface morphologies and chemistries to interact with the living systems or to actively induce a biological response also by the release of drugs or proteins. These customized requirements foster technologies that can be implemented in additive manufacturing systems. Here, we present a novel approach based on spraying processes that allow to control separately topographic features in the submicron range (~60 nm to 2 μm), ammine or carboxylic chemistry, and fluorophore release even on temperature-sensitive biodegradable polymers such as polycaprolactone (PCL). We developed a two-steps process with a first deposition of 220 nm silica and poly(lactic-*co*-glycolide) (PLGA) fluorescent nanoparticles by aerosol followed by the deposition of a fixing layer by an atmospheric pressure plasma jet (APPJ). The nanoparticles can be used to create the nanoroughness and to include active molecule release, while the capping layer ensures stability and the chemical functionalities. The process is enabled by a novel APPJ which allows deposition rates of 10−20 nm·s^{-1} at temperatures lower than 50 °C using argon as the process gas. This approach was assessed on titanium alloys for dental implants and on PCL films. The surfaces were characterized by Fourier transform infrared, atomic force microscopy, and scanning electron microscopy (SEM). Titanium alloys were tested with the preosteoblast murine cells line, while the PCL film was tested with fibroblasts. Cell behavior was evaluated by viability and adhesion assays, protein adsorption, cell proliferation, focal adhesion formation, and SEM. The release of a fluorophore molecule was assessed in the cell growing media, simulating a drug release. Osteoblast adhesion on the plasma-treated materials increased by 20% with respect to commercial titanium alloy implants. Fibroblast adhesion increased by a 100% compared to smooth PCL substrates. The release of the fluorophore by the dissolution of the PLGA nanoparticles was verified, and the integrity of the encapsulated drug model was confirmed.

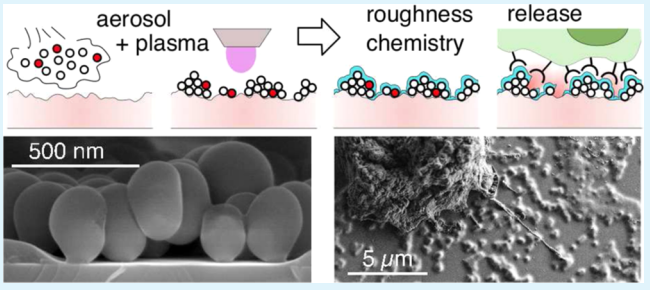

KEYWORDS: *nanostructures, atmospheric pressure plasma, chemical functionalization, scaffolds, active molecule release*

1. INTRODUCTION

Implant technology, stimulated by tissue engineering advances, has faced in the last years an always increasing complexity. The driving force has been the chase of mimicking biosurfaces in order to improve scaffold or prosthesis integration in tissues.[1] However, the accurate replication of the biological surfaces is a challenging task because materials and structures are difficult to emulate and their mechanisms are still not fully understood.[2] The pivotal features of an implant, which have been found to influence cell growth and differentiation on the implant surfaces, are mainly three: the geometrical and mechanical properties, the surface chemistry, and the surface topography.

The mechanical properties, mainly the scaffold stiffness, are bulk characteristics and are known to guide cell differentiation and growth through mechanotransduction.[2] The geometrical shape, for example, pore interconnection, influences also vascularization and cell motility, driving their growth on preferential directions or improving differentiation.[3]

Received: September 12, 2018
Accepted: October 25, 2018
Published: October 25, 2018

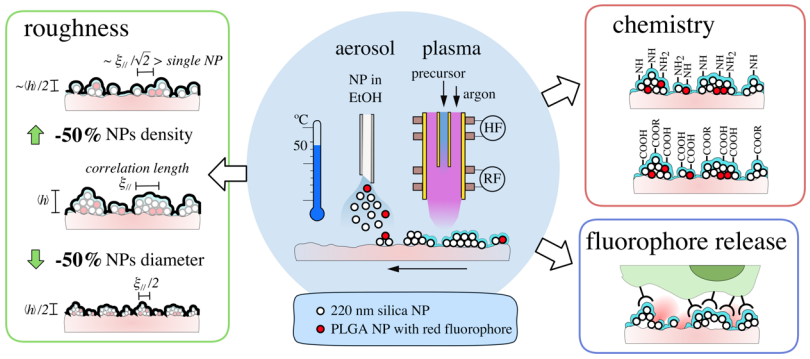

Figure 1. Scheme representing the proposed technology and its control of roughness, chemistry, and molecules release. In the center, the deposition process is summarized with the aerosol deposition of the NPs and the following deposition of a fastening layer by APPJ, scanning the samples. The film properties are controlled independently: the roughness is controlled laterally and vertically by NPs size and density in the submicron range; the surface chemistry of the deposited APPJ plasma polymer can offer amine or carboxylic functionalities by the precursor choice; during cell growth, when PLGA NPs with a red fluorophore embedded are used, the fluorophore is released in the culture media.

For the surface chemistry aspect, usually, the surfaces have to maintain a moderate hydrophilicity (contact angle 40−60°);[4] negative charge on surfaces improves the proliferation, while positive charge increases spreading and differentiation.[5,6] The desired surface chemistry is often obtained by wet chemistry processes or by the use of silane agents. However, in the last years, the atmospheric plasma technology is no more confined to the mere activation of the surface,[7,8] but it is consolidating for the deposition of stable functional coatings[9−11] even on three-dimensional (3D) structures.[12] The surface chemical groups influence mainly the protein adsorption[13] by their polarity and by covalent bonding, inducing a selection also on their folding and orientation.[14]

The topography effects can be divided into two main ranges: micrometer and nanometer scales. The roughness of the same order of magnitude of cell size influences mainly their adhesion, and the presence of a preferential orientation can also drive their motility and growth in the desired directions.[15] Microscale roughness is also known to favor osteoblasts growth due to the enhanced precipitation of minerals in the micropores.[1] Because of these evidences, for example, a large number of commercial dental implants presents sand-blasted and acid-etched (SBAE) surfaces, showing microscale porosity. The nanoroughness superposes a further control because cells feel the nanoscale features owing to their filopodia.[2,16] Preferentially disordered structures with a critical distance of the features of 60−70 nm allow the binding of integrins to the surfaces and their maturation to focal adhesion (FA) point with their clustering in groups at least of 7−8 proteins.[17−19] The roughness in the range of few tens up to few hundreds of nanometers is a key factor in cell interaction with the implants.[20,21] Rounded shapes in this range allow also to increase tension stress in FA points influencing the mechanotransduction signal chain and are demonstrated to influence cell differentiation and growth.[19] However, it is always difficult to decouple the effect of the surface nanotopography and chemistry because the production processes affect both concurrently;[22] moreover, the suitable technologies depend on scaffold materials and can encounter limitations on centimeter scale and on 3D shapes.[23−25]

Furthermore, the next generation of implants requires smarter features such as the possibility to create topographic or chemical gradients to guide cell growth in the scaffold[2,26] or to release ions or active molecules.[6] For example, in bone implants, the presence of antibacterial coatings can prevent infections and therefore prosthesis loosening,[27] the release of ions like Ca and Sr improves osteoblast growth,[28] and the delivery of proteins, such as growth factors, induces cell differentiation.[29]

Scaffold production technologies are still under continuous development to satisfy the complexity of desired features for more functional tissue regeneration.[30−32] Despite the different fabrication methods and materials available, a localized control over the topographic and chemical functionalization aspects is an open challenge. As an example, titanium-based prostheses are characterized by acid etching and anodization processes for micro- and nanoroughness production, respectively, but it is still quite difficult to impart a nanostructure gradient with these methods.[1,33] In a similar way, on polymers, the nano- and microstructures induced by solvent and particulate leaching[1,34] or surface solvent etching[25] affect the whole scaffold. On the other side, the lithographic technologies find some constraints in centimeter scale 3D scaffolds.[35] However, some first attempts are presented in the literature for surface chemistry gradient control on polymers using graphed hydrophilic groups[26] or inducing the gradient from the surface to the inner core thanks to plasma processes in vacuum[12,36] or in atmosphere.[37]

Here, we present a novel approach to tackle surface chemistry and topography based on a two-step spraying technique: at first, nanoparticles are deposited by aerosol of a dispersion, and second, a fixing layer is deposited by an atmospheric pressure plasma jet (APPJ). In order to highlight the potential of this technology, we present its effects on cell growth tested on two different substrates: grade 2 titanium for dental implants and a thermal-sensitive polycaprolactone (PCL) 20 μm thick film. For the two substrates, we used different cell lines, preosteoblasts and fibroblasts, the first for an application-oriented testing (bone tissue engineering) and the latter for their lower sensitivity to nanotopography.[38] Drugs or protein release can be achieved by the use of bioresorbable nanoparticles embedding the active molecules. In this way, the smart additive is protected by plasma reactive ions and radicals, and it can be incorporated in the coating without being altered.[39] Moreover, the introduced plasma process allows to select protein, drug or mixture, and which size of particles to use independently. This drug release functionality is investigated using fluorescent nanoparticles of

DOI: 10.1021/acsami.8b15886
ACS Appl. Mater. Interfaces 2018, 10, 39512−39523

poly(lactic-*co*-glycolide) (PLGA). The presented technology offers an easy way to tailor the scaffold surfaces, allowing to precisely control key properties such as surface chemistry, roughness, and drug release, addressing them separately (Figure 1). Because of substrate temperatures lower than 50 °C during the plasma process, the surface morphology of thermal-sensitive materials is preserved even at the nanoscale. The fixing layer, which is few hundred nanometers thick, appears like a permeable well-adherent snowfall on the nanostructures. As the whole process is based on spraying techniques, it can be implemented on 3D printers allowing the design of gradients.

2. EXPERIMENTAL SECTION

2.1. Sample Preparation. *2.1.1. Atmospheric Pressure Plasma Jet.* The low temperature of plasma polymer layer deposition was achievable, thanks to an innovative design of the jet device (Plasma Stylus Noble, Nadir srl) that couples two generator frequencies: 17 kHz and 27 MHz.[40] The jet is based on a double dielectric barrier discharge scheme with a double couple of ring electrodes positioned externally to an alumina tube and powered the upstream couple with an high voltage at kHz and the downstream at MHz, respectively (Figure 1). The jet uses argon as the process gas. A schematic representation of the atmospheric pressure plasma complete deposition system is available in the Supporting Information (Figure S2). This configuration assured deposition rates of 10−20 nm·s^{-1} at temperatures lower than 50 °C avoiding the use of helium. For the experiment, Ar 5.0 purity was used as the process gas (Sapio Ar 5.0 purity, 4.5 slm), and nitrogen (Sapio N_2 5.0 purity) was flushed, thanks to an outer coaxial duct at 10 slm to confine the process atmosphere and avoid oxygen content in the plasma area. On the other side, the chemical precursors were introduced by an inner alumina capillary just before the RF electrodes (Figure 1).

2.1.2. Substrate Preparation. Grade 2 commercially pure titanium samples of cylindrical shape (ø 7 mm, height 3 mm) were supplied by Titanmed S.R.L. with different surface finishing: T1 as worked by lathe, that is, machined and T2 sand-blasted (large grit)—acid etched (SBAE). The samples were cleaned with acetone and rinsed with isopropanol/H_2O solution 70% and then were sterilized in an ultrasound bath for 5 min in isopropanol and rinsed in Milli-Q water. The root mean square (RMS) roughness (R_{rms}) for T1 samples was about 110 nm in a scanning area of 40 × 40 μm (Supporting Information Figure S1), while T2 sample roughness is in the micrometer range.

PCL films (440744 Aldrich, average M_n 80 000) were produced by hot moulding. The mirror polished surface of the Si(100) wafers was functionalized by spinning a solution of perfluorodecyltriethoxysilane (FAS-17, Aldrich 658758, purity 97%) 1% in ethanol followed by drying in oven in air at 250 °C. Two silicon wafers was then used as moulds introducing between them 300 mg of pellets at 90 °C and applying a pressure of about 70 kPa. The films obtained were about 20 μm thick characterized by a spherulite surface structure[41] with a RMS roughness of about 50 nm in a scanning area of 40 × 40 μm (Supporting Information Figure S1). The PCL films were then cut in discs (ø 1 cm).

2.1.3. Aerosol Nanoparticle Deposition. Monodispered silica nanoparticles were synthesized using the Stöber process[42] starting from tetraethyl orthosilicate (131903 Aldrich, purity 98%), ammonium hydroxide solution (338818 Aldrich, 28% NH_3 in H_2O), and ethanol (EtOH, 1.00983 EMD Millipore) in the proportion of 1:3:42. The solution was left covered under stirring overnight at 30 °C. The resulting particle average size was about 220 nm with a full width at half-maximum of 10 nm. Scanning electron microscopy (SEM) images and size distribution are presented in the Supporting Information (Figure S4). The particles were rinsed in deionized water in an ultrasound bath three times and then redispersed at 0.5 wt % in EtOH.

In order to test the possibility to release active molecules, red fluorescent nanoparticles of PLGA were supplied by Phosphorex (Degradex LGFR200, excitation 652 nm/emission 668 nm). The particles, of 200 nm of nominal diameter, were dispersed by an ultrasonic bath at 0.5 wt % in EtOH just prior the aerosol deposition. SEM imaging was used to verify the dispersion particle with the deposition of a solution drop on the silicon substrate, and the size distribution of the particle appeared broad with a PDI of about 0.4 (Supporting Information Figure S13).

The deposition via aerosol was performed using a plotter and air pressure nebuliser.[43] The plotter was moved at 50 mm·s^{-1} in parallel scanning lines with a step of 1 cm. The nozzle distance from the samples was set to 8 cm, and the suspensions were dosed by a syringe pump at 2 mL·min^{-1} and sprayed by a 3 bar air flux. The substrates were kept at 40 °C on a hot plate to increase the EtOH evaporation rate without affecting the substrates.

2.1.4. Plasma Polymer Deposition. For the fixing layer deposition, the APPJ was mounted on the same plotter of the aerosol nozzle at a distance of 2 mm from the substrates. As in Mussano et al.,[10] two different coatings were deposited and characterized by opposite polarities: positive polarity with amine groups using 3-aminopropyltriethoxysilane (3-APTES, Sigma-Aldrich, ≥98%) as a precursor and negative polarity with carboxylic/carboxylate groups starting from methylmethacrylate (MMA, Sigma-Aldrich, ≥99%). The precursors were introduced in the plasma, using the inner capillary just prior the RF electrodes, fluxing Ar in a bubbler containing the liquid monomer at room temperature. For all the processes, the power supply at about 17 kHz is set to an output of 8−9 kV peak-to-peak at about 8 W, while the RF power is adapted depending on the substrate using also pulsing mode. The process parameters are presented in the Supporting Information (Table S1). For Fourier transform infrared (FT-IR) analyses in transmission mode, the coatings were deposited also on silicon (100) substrates. The deposition rates for all the coatings were in the 10−20 nm·s^{-1} range.

2.2. Surface Characterization. *2.2.1. Scanning Electron Microscopy.* The SEM was used to investigate the morphology of the deposited nanostructures and how they relate to cell growth (FE-SEM ZEISS Sigma VP and HD). The samples were observed at low accelerating voltages (≤5 kV) in order to avoid metallization. Sample cross sections on silicon wafers were obtained by crack propagation on the substrate at room temperature. The osteoblasts on titanium substrates were fixed with 1% glutaraldehyde (Sigma G7776) buffered in 0.1 M sodium cacodylate (Agar, UK) (4 °C, 1 h) after a 24 h incubation period to achieve a suitable cell density for SEM observation of individual cell morphology. Then, cells were dehydrated through a series of ethanol/water solution from 20 to 100% ended with hexamethyldisilazane (Sigma) soaking and air-drying. The fibroblast cells on PCL films were fixed with 1% glutaraldehyde (Sigma) buffered in 0.1 M sodium cacodylate (Agar, UK) (4 °C, 1 h) after 4 days of incubation period. The samples, after washing, were soaked in a solution of 1-butyl-3-methylimidazolium tetrafluoroborate 2.0% in Milli-Q water (Sigma) for 60 s at room temperature; the excess of solution was removed by a pipette followed by drying in a nitrogen flux.

2.2.2. Atomic Force Microscopy. Surface topography was characterized by atomic force microscopy (AFM, model NT-MDT Nova Solver-PRO) in tapping mode. The data were analyzed by Gwyddion software leveling the data only by flat plan subtraction and a following row alignment using the median differences tool. The two-dimensional (2D) radial power spectral density function ($W_r(k)$) has been used to describe the roughness as a function of spatial frequencies.

2.2.3. FT-IR Spectrophotometry. Silicon wafer-coated samples were used for transmission FT-IR spectrophotometry characterization. Measurements were performed by using a PerkinElmer Spectrum One spectrophotometer by performing 32 scans for each sample.

2.3. Biological Characterization. *2.3.1. Protein Adsorption.* To quantify the amount of protein adsorbed, the titanium disks were incubated in the presence of fetal bovine serum in phosphate buffered

DOI: 10.1021/acsami.8b15886
ACS Appl. Mater. Interfaces 2018, 10, 39512−39523

saline (PBS) at 2% concentration, at 37 °C for 30 min. Subsequently, the samples were washed twice with PBS, and the adsorbed protein was eluted from the disks using tris(hydroxymethyl)aminomethane (Tris) Triton buffer [10 mM Tris (pH 7.4), 100 mM NaCl, 1 mM ethylenediaminetetraacetic acid, 1 mM ethylene glycol tetraacetic acid, 1% Triton X-100, 10% glycerol, and 0.1% sodium dodecyl sulfate (SDS)] for 10 min. The total protein amount was quantified using SERVA BCA Protein Assay Micro Kit (SERVA Electrophoresis GmbH, Heidelberg, Germany) and Pierce BCA Protein Assay Kit (Life Technologies, Carlsbad, California, USA) following the manufacturer's instructions.

2.3.2. Cell Assays. To study the biological response in vitro, preosteoblastic murine cells (MC3T3-E1, ECACC, Salisbury, UK) and primary skin fibroblasts were used. MC3T3-E1 cells and fibroblasts were maintained in α minimum Eagle's essential medium and Dulbecco's modified Eagle's medium, respectively, supplemented with 10% fetal bovine serum (Life Technologies, Milan, Italy), 100 U·mL^{-1} penicillin, 100 μg·mL^{-1} streptomycin. Both cell types were passaged at subconfluency to prevent contact inhibition and were kept under standard culture conditions (humidified atmosphere of 5% CO_2 in air, at 37 °C). Culture and experimental conditions were previously established in our laboratories and adapted to areas of different tested surfaces.

2.3.3. Cell Adhesion. Osteoblast adhesion was evaluated on titanium samples using a 24-well plate (BD, Milan Italy) as support. Cells were detached using trypsin for 3 min, carefully counted, and seeded at 3×10^3 cells/disk in 100 μL of growth medium on the disks with different roughness values. The 24-well plates were kept at 37 °C, 0.5% CO_2 for 10 min. Before and after fixation in 4% paraformaldehyde in PBS for 15 min at room temperature, cells were washed two times with PBS and then stained with 1 μM 4′,6-diamidino-2-phenylindole, dilactate (Molecular Probes, Eugene, California, USA) for 15 min at 37 °C to visualize cell nuclei. Images were acquired using a Nikon Eclipse T-E microscope with a 40× objective. The cell nuclei were counted using the "Analyze Particles" tool of NIH ImageJ software (ImageJ, U. S. National Institutes of Health, Bethesda, Maryland, USA, http://imagej.nih.gov/ij/).

Fibroblast adhesion was assessed using 3-(4,5-dimethylthiazolyl)-2,5-di-phenyltetrazolium bromide (MTT) test. PCL films with or without coating or nanoparticles (NPs) were incubated with 100 000 fibroblasts/samples in 250 μL culture medium. Samples were incubated at 37 °C for 15 min, rinsed in PBS to remove nonadherent cells, and added with MTT for 4 h. Reaction was stopped by acidification, and the optical density was spectrophotometrically recorded. A standard curve prepared by seeding decimal dilution of cells was used to calculate the cell number. Data are reported as ratio over nonfunctionalized substrates.

2.3.4. Cell Viability. To assess the viability, MC3T3-E1 cells were plated at a density of 2500 cells/sample in 24-well culture dishes, at 1, 3 and 7 days, using CellTiter-Glo (Promega, Milan, Italy). The CellTiter-Glo luminescent cell viability assay quantifies viable cells owing to the adenosine 5′-triphosphate (ATP) content. The amount of ATP is indeed directly proportional to the cell number.

Fibroblasts (100 000/samples) were cultured for 24 h at 37 °C, washed, and then incubated for 4 h with MTT to assess metabolic activity in viable cells.[44] Reaction was stopped and recorded as described above. A standard curve prepared by seeding decimal dilution of cells was used to calculate the number of viable cells.

2.3.5. Cell Proliferation. Fibroblasts were labeled with a CFSE cell tracker (carboxyfluorescein succinimidyl ester; Thermo Fisher), a green fluorescent dye retained within cells for long periods, and cultured on PCL films with or without coating or NPs at 37 °C for 7 days. Once incorporated within cells, the dye is not transferred to adjacent cells, but it halves within daughter cells, thus following each cell division up to 7−8 divisions. Percentage of positive cells was quantified by fluorescence-activated cell sorting analysis.

In a parallel set of experiments, CFSE-related fluorescence was visualized by confocal microscopy. Briefly, after 7 days, culture cells were fixed in 4% paraformaldehyde for 15 min at room temperature, washed twice in PBS, and mounted in a drop of mounting media (Sigma). Samples were analyzed and photographed using a Leica TCS-NT/SP2 confocal microscope.

2.3.6. Focal Adhesion. Fibroblasts were cultured on PCL films with or without coating or NPs for 24 h at 37 °C. For Western blot analysis, total proteins were extracted in radioimmunoprecipitation assay buffer (150 mM NaCl, 50 mM Tris-HCl, 0.25 w/v % sodium deoxycholate, 0.1% Nonidet P-40, 100 μM $NaVO_4$, 1 mM NaF, 1 mM phenylmethylsulfonyl fluoride, 10 μg·mL^{-1} aprotinin, 10 μg·mL^{-1} leupeptin). Particulate material was removed by centrifugation, and proteins (25 μg/line) were separated with 10% SDS polyacrylamide gel electrophoresis and then transferred to nitrocellulose membranes. Membranes were probed with anti-FAK phospho Y397 antibody (clone: EP2160Y; Abcam) and then incubated with the proper HRP-conjugated secondary antibodies. Control loading was performed using anti-β-actin antibody (Sigma). Bands were visualized using enhanced chemiluminescence (Millipore). Images were captured using Hyperfilm MP (GE Healthcare), and densitometry analysis was performed using NIH ImageJ software.

2.3.7. Statistical Analysis. Results are reported as mean ± SEM of two independent experiments, each performed in triplicate. Statistical analysis was performed using GraphPad Prism 3.03 (San Diego, California, USA). Statistical significance was calculated using one-way analysis of variance test followed by the Newman−Keuls post-hoc test; $p < 0.05$ was considered statistically significant.

3. RESULTS AND DISCUSSION

3.1. Nanostructured Coating Design. The technology proposed here aims to decouple the roughness and surface chemical functionalization on any substrate at low temperature. The process involves two steps: particles spraying followed by an APPJ layer deposition to fasten the NPs to the surface (Figure 1). As a first step, silica monodispersed particles of 220 nm in diameter were selected as a building block to create controlled roughness. The choice of such size is due to the expected size of the FA points of the cells on the surfaces that is of the order of few hundreds of nanometres. For the maturation of a stable FA point, indeed, it is needed at least the clustering of 6−7 integrins, with proteins spacing of some tens of nanometres.[17] Moreover, the rounded surface would introduce further tension stress to the connections, facilitating the FA widening.[19] The particles were dispersed in ethanol at 0.5 wt % and then sprayed as an aerosol on the surfaces. The use of the alcohol was due to its higher vapour pressure in order to avoid the "coffee rings" effect[45] of the drops evaporating on the surface.

As a second step a plasma polymer layer was deposited by an atmospheric plasma jet on the particles. The role of the coating is twofold: to fix the particles on the surface, assuring particles adhesion and therefore roughness stability, and to offer the desired chemical functionalization. In this work, we used similar coatings of the ones presented in Mussano et al.[10] that showed chemical and mechanical stability after ageing for 48 h in water solution and after UV sterilization. A 30% reduction of the RF average power was carried out to adapt the process to the substrates (Supporting Information Table S1). The plasma was driven in pulsed mode at a frequency of 500 Hz and duty cycle of 50% for the titanium substrate to further reduce potential substrate heating due to cylinders corners. However, the average power was kept equal to the one used in continuous mode on PCL and the FT-IR spectra can be nearly overlapped (Figure 2a). The thermal load of the plasma process was evaluated by the heating of a copper mass in place of the samples in static conditions,[46] and the thermal power resulted is about 185 ± 30 mW (Supporting Information Figure S7), which is in the range of jets used in plasma

DOI: 10.1021/acsami.8b15886
ACS Appl. Mater. Interfaces 2018, 10, 39512−39523

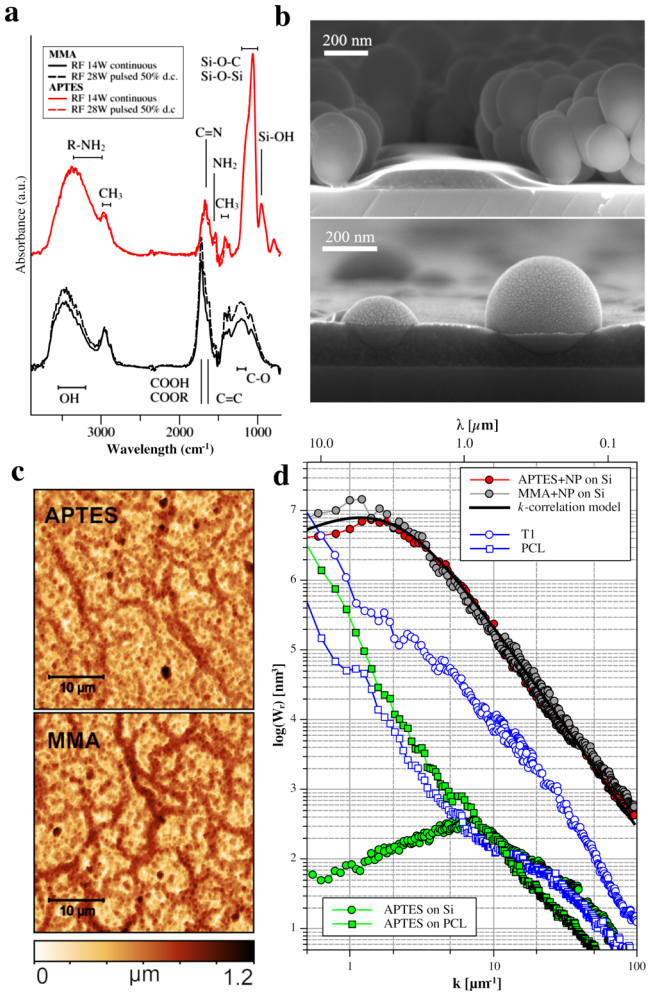

Figure 2. (a) FT-IR spectra of the plasma polymers deposited on silicon starting from MMA and APTES precursors using the parameters for titanium and PCL substrates. (b) SEM cross-sectional images of the SiO_2 (ø 220 nm) (top) and Degradex PLGA (bottom) NPs deposited on a silicon wafer and coated with the APTES plasma polymer. (c) AFM topography of the two-step process on the silicon substrate. (d) Radial power spectral density $W_r(k)$ of two-step processes on silicon with different chemical functionalities overlapped with the fitted *k*-correlation model curve. For comparison are added the $W_r(k)$ of the T1 and PCL substrates and of the APTES plasma polymer on Si and PCL substrates.

medicine applications.[47] The deposition rates were about 20 nm·s^{-1} for the MMA and 10 nm·s^{-1} for APTES precursors.

The results of this two-step deposition process can be observed in the cross section in Figure 2b. The particles appeared covered by a plasma polymer about 100 nm thick: a thicker layer was observed on the top of the particles, while it decreased when getting closer to the substrate because of a shadowing effect of the particles themselves. Therefore, the coating thickness was less uniform than in vacuum processes.[42] Nevertheless, the coating was present even at the base of the particles, gluing them to the substrate. Indeed, the atmospheric pressure nature of the plasma deposition assures an isotropic flow of the radicals. Therefore, the thickness is determined mainly by the local acceptance angle: the top of the particle is exposed to more than a semiplane of incoming radicals, while the substrate below the particle sees its semiplane partially occupied by the particle itself. Moreover, as the coating grows, the acceptance angle for shadowed areas further decreases because of the coating grown on the upper part and the one grown on the substrate get in contact. As can be observed by the SEM cross section (Figure 2b bottom), no voids could be detected at this later growth stage between the coating on the particle and on the substrate. However, a geometrical junction is always visible and suggests anyhow the presence of discontinuities in the coating. Therefore, in order to ensure a good adhesion of the particles on the surfaces, the fixing layer must have the same thickness of the particle radius. At the same time, the presence of these defects around the particles guarantees coating permeability, which can be tailored just by controlling its thickness.

The particles were randomly positioned, leaving part of the substrate area free or arranging up to in stack of no more than three levels. The presence of substrate areas free of particles is needed to allow the particle fastening by the coating. However, the fixing layer successfully bonded also the particles to each other, when at least part of each was in view of the plasma (Supporting Information Figure S6). Particles in the lower levels, if fully shadowed by the others, could not be coated, resulting in a loss of mechanical stability. Because of that effect if all the surface would be covered by three layers, no anchoring to the substrate can be achieved. Therefore, the choice of particles size is relevant in order to reach the desired roughness range with a limited number of particles deposited.

In Figure 2a, the FT-IR spectra of the fixing coatings are presented, showing for the MMA and APTES precursors the presence of the functional carboxyls/esters and amino groups, respectively. The layers were deposited by a plasma-enhanced chemical vapor deposition process at atmospheric pressure; therefore, their chemical structure is related to plasma parameters. The condensation of the coating on the surface is obtained via the creation of precursor's fragments along the interaction with plasma reactive species and by their reaction and recombination in the gas phase and on the surface.[48] As a matter of fact, the resulting coating is characterized by a branched network of heterogeneous molecules. However, depending on the selected process parameters, chemical radical or ionic chain growth can still be present, allowing to preserve, at short range, the chemical structures of analogous polymer obtained by wet chemistry.

For the coatings obtained with the APTES precursor, nitrogen-containing groups are visible as primary amines at 1558 cm^{-1}, at 1660 cm^{-1} as stretching vibration of the oximes, and at 3200−3400 cm^{-1} as amides. The presence of the primary amines, together with the $CH_{2,3}$ stretching vibrations visible at 2980−2880 cm^{-1}, confirms the retention of some aminopropyl chains of the precursor.[10] The presence of oximes and amides is probably due to precursor oxidation during the deposition process, as supported also by the presence of the hydroxyls groups at 3000−3500 cm^{-1}. The oxygen was dragged in the plasma region by the jet movement on the plotter even if nitrogen was fluxed in the outer duct of the torch to confine the process atmosphere. Nevertheless, the precursor oxidation was partially prevented as shown also by the methyl groups visible at 1465−1375 and 2980−2880 cm^{-1}. Moreover, the silica coating backbone is recognizable in the FT-IR spectra at 1200 and 1000 cm^{-1} that prevents its dissolution in aqueous media.[49,50]

The MMA precursor was used to obtain carboxylic acid surface chemical functionalities. In this case, the process is adjusted in order to produce carboxyl groups, thanks to

DOI: 10.1021/acsami.8b15886
ACS Appl. Mater. Interfaces 2018, 10, 39512−39523

chemical reactions. During the deposition process, the precursor is fragmented leading to the formation of aldehydes and ketones.[51] The oxidation of the aldehydes during the process can lead to the formation of the carboxyl groups.[51] This reaction process is supported by the FT-IR spectra obtained, where a broad absorbance peak centered at 1720 cm^{-1}, related to the C═O carbonyl group, can be preferentially attributed can be preferentially attributed to carboxyl groups (absorbing in the range 1700−1725 cm^{-1}) rather than to esters (1730−1735 cm^{-1})[52] and to the presence of ketones (1705−1720 cm^{-1}) and aldehydes (1730−1740 cm^{-1}). The presence of the carboxyl groups is suggested also by the intense OH vibration band between 3200 and 3500 cm^{-1}. Part of the methyl groups coming from the precursor was maintained saturated in the coating as can be deduced by the presence of the adsorption signal at 2850−3000 cm^{-1} and its absence in the 800−1000 cm^{-1} range.[51] The C═C signal at 1635 cm^{-1} is frequently observed in MMA plasma-deposited coatings and is related to unsaturated structures that may form during the plasma process.[53] However, in order to verify the electrophilic character of the coating, the toluidine blue O test was performed,[54] obtaining a density of negatively charged groups of about $4.8 \pm 0.6 \times 10^{14}$ cm^{-2}.

Hence, the two plasma polymers offer two different surface chemistries and are not influenced by substrate material or morphology. In Figure 2c, the topographies obtained for the two fixing layers are shown. Both surfaces showed an average height of about 500 nm with respect to the substrate and a RMS roughness (R_{rms}) of 180 nm, which confirms that the particles are distributed on average in two levels. At the smaller scale scanning range, the single particle as roughness building blocks could be observed (Supporting Information Figure S8). In order to study the roughness as a function of the spatial frequency, the radial power spectral density ($W_r(k)$) of the roughness, which corresponds to the 2D Fourier transform of the autocorrelation function integrated over all the angles, was calculated (Figure 2d). For the analysis, AFM measurements at different scanning ranges from 5 × 5 up to 80 × 80 μm were recorded. The $W_r(k)$ of the samples with MMA and APTES coatings on the nanoparticles fully overlap and is characterized in a log−log scale by a linear slope at higher spatial frequencies and then saturates forward lower frequencies.

This behavior is characteristic of a self-affine structure of the surface[55] and is related to the production process of the roughness. The silica NPs are the building blocks of the growing interface and added one by one produce a fractal structure that is usually represented by the following scaling form

$$\sigma^2(L, h) = L^{\alpha} f(h/L^{\alpha/\beta}) \quad (1)$$

where σ is the variance in the surface height, h is the deposit thickness, and L is lateral size of the system in simulation models, all parameters in unit of the building block.[56] The lateral size in real surfaces can be associated to the correlation length $\xi_{\parallel}$, which depends at the same time on h, slowly increasing as the thickness increases. The scaling function $f(x)$ has a constant value for $x \gg 1$ and has the form $f(x) \approx x^{\beta}$ for $x \to 0$. Therefore, as the particle deposition process proceeds, the roughness of the surface rises up to a certain saturation value:[57] the higher the β, the faster is the increase; on the other side, $\xi_{\parallel}$ acts as a threshold limit for this scaling expansion. The $\xi_{\parallel}$ is related to the relaxation processes during the growth as the interactions among the spheres.[58]

The $W_r(k)$, reflecting the same features of eq 1, can be used to evaluate the different scaling parameters. By fitting the linear part in the log−log scale with the function $W_r(k) \propto k^{-2(\beta+1)}$, the β exponent is retrieved together with the fractal dimension as $D_f = 3 - \beta$.[59] For all the deposited structures, we obtained $\beta = 0.45 \pm 0.05$ and $D_f = 2.55 \pm 0.05$, which are in agreement with the 3D simulations where the diffusion-limited aggregation mechanism and no long-range interactions are considered.[60] These hypotheses well fit with our deposition mechanism, where the use of ethanol and of a mild heating avoids surface wetting, limiting the possibility of a long-range rearrangement. Therefore, taking into account the self-affine surface behavior, the topography evolves following the scaling law $h(bx) \approx b^{D_f-2} h(x) \approx \sqrt{b}\, h(x)$, which means, for example, that a lateral scaling of a factor 4 in building block units leads to a factor 2 in height. At the same time, the roughness is related to mean deposit thickness as $\sigma \approx \langle h \rangle^{\beta} \approx \sqrt{\langle h \rangle}$.[56]

The whole $W_r(k)$ with its saturated part can be studied modeling an isotropic autocorrelation function, which allows to introduce a correlation length. The k-correlation model[61] considers for the autocorrelation function a continuous transition model between exponential and Gaussian. For the radial power spectral density, the corresponding fitting equation is

$$W_r(k) = \frac{\sigma^2 \xi_{\parallel}(\xi_{\parallel} k)}{(1 + (\xi_{\parallel} k)^2)^{\beta+3/2}} \quad (2)$$

where for $\beta = 0$, the autocorrelation function decreases exponentially, while for $\beta \gg 0$, it gets close to a Gaussian behavior. The advantage of this k-correlation model is the possibility to identify $\xi_{\parallel}$.

In Figure 2d, the fitting result is presented with a $\xi_{\parallel} \simeq 800$ nm, which is close to 3 units of building block, and it is expected to slowly increase with layer growth.[57] For lateral frequencies lower than $\xi_{\parallel}^{-1}$, the roughness reached a saturation value and was constant. The $W_r(k)$ functions of the PCL films and the T1 titanium substrate, as well as the positive polarity coating on PCL and on silicon substrates, are presented for comparison. It can be observed that in the submicron lateral range, both substrates had roughness more than an order of magnitude lower and that even the effect of the coatings was irrelevant. Moreover, the roughness introduced by the fixing coatings is visible only on the Si substrate that is nearly atomically flat, and it showed an overall R_{rms} of about 4 nm. Therefore, the developed process selectively controls the roughness in the submicron range by the choice of the building blocks size, which defines the fractal basic unit. By setting the desired spatial roughness as $\xi_{\parallel}$, the use of building blocks few times smaller than $\xi_{\parallel}$ allowed us to reach efficiently the designed value only with one or few layers of particles deposited. This ensures the possibility to fix the particles on the surface. At the same time, the roughness on the vertical scale propagates as the square root. It has to be considered that the increase of the number of layers increases the $\xi_{\parallel}$ and the overall roughness but does not influence the roughness height on the lateral scale lower than $\xi_{\parallel}$. Therefore, the choice of the building block size close to the required spatial roughness maximizes also the roughness height in the same range.

The nanostructures have been obtained on 2D substrates, but in principle, they can be obtained also on 3D geometries as just room temperature spraying techniques at atmospheric

DOI: 10.1021/acsami.8b15886
ACS Appl. Mater. Interfaces 2018, 10, 39512−39523

pressure are involved. Moreover, as feasible outlook, the proposed process can be implemented directly on a 3D printing biopolymer platform in order to locally functionalize and control the nanostructures.

3.2. Osteoblast Growth. The biological response in vitro on titanium substrates was characterized using the widely diffused preosteoblastic murine cell line MC3T3-E1.[62] The substrates considered had two different surface finishing: T1 was after the machining process with an R_{rms} of the order of a hundred of nanometres, while T2 was after a following sand blasting—acid etch process (SBAE) and presented a R_{rms} > 2 μm. Therefore, the direct comparison between the results on T1 and T2 allows to highlight the effect of the microscale roughness and its interaction with the deposited nanostructured coating.

At first, the cell viability was evaluated by CellTiter-Glo assay.[63] The T1 and T2 substrates showed, with and without the coatings, similar results (Figure 3a). This comparison

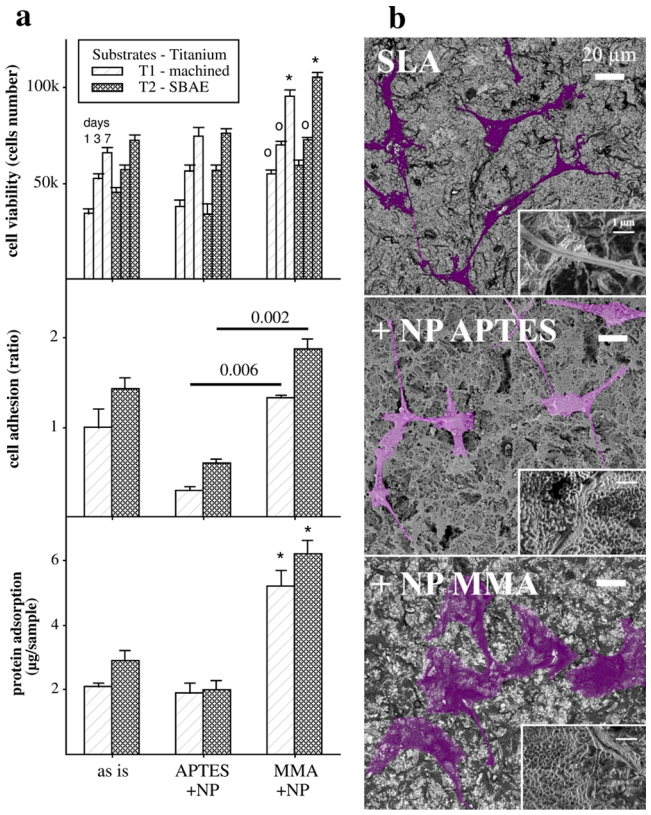

Figure 3. (a) Results on viability (1, 3, and 7 days), protein adsorption, and cell adhesion for titanium T1 and T2 substrates as is and with the deposited nanostructured layer with the two different chemical functionalizations: amino groups starting from APTES and carboxyl groups using MMA (* 0.001 vs as is; ○ 0.01 vs as is) and (b) SEM images with a backscattering detector to highlight cells morphologies on T2 substrates as is and coated (in the insets, higher magnification images obtained with the in-lens detector).

highlights the fact that the microroughness in this case seemed not to influence the survival of the cells in all the assessed time points, which increased along time consistently with a noncytotoxic behavior of all the considered surfaces.[64] The addition of the nanostructured coatings on both T1 and T2 substrates did not affect the cell viability, which was even enhanced by the deposition of the nucleophilic functionalities.

A similar trend with no differences between T1 and T2 substrates could be observed for protein adsorption, with and without the coatings. This behavior was expected, indeed, because the surface chemistry is known to mainly influence the protein adsorption and folding.[2] The main difference is in fact related to the threefold enhancement of the adsorption on surfaces with carboxylic functionality. The same behavior was found on flat titanium substrates applying the same plasma polymers without nanostructures.[10] In that case, the increase was only of about the 50%; therefore, the enhancement of this effect could be a first evidence of a synergistic action of nanoscale roughness and chemistry.

Cell adhesion seems to be more sensitive to the various chemical and morphological effects. In fact, the formation of the FA points and protein interaction with the surface is the starting point of a communication chain that guides to cell proliferation and differentiation. As pointed out in Mussano et al.[10] using the same functional coatings and the same cell line, the amino groups on the surface led to a reduction of the proliferation and an improvement in osteogenesis differentiation verified by cell spreading and tapered morphology and by osteocalcin detection. On the other side, the carboxyl groups led to a higher proliferation and to chondrogenic differentiation. These results are widely supported in the literature using as well other surface functionalisation techniques.[9,13] Also, in Figure 3a, we can observe the positive effect on cell adhesion of the nucleophilic surfaces opposed to an evident repression on electrophilic samples. The positive effect of the carboxyl groups is of the same order of magnitude of what obtained on flat substrates and therefore is mainly due to a surface chemistry effect. On the other side, the negative effect of the amino groups was strongly accentuated by the nanoscale roughness. Cell growth is always in competition with the differentiation. Therefore, because the nanoroughness with the selected spatial frequencies is expected to strongly influence the formation of the FA points, it is not surprising that we observed less proliferation.[21,22]

In cell adhesion, we observed also a significant difference between T1 and T2 substrates in all the conditions considered. This effect can be interpreted as general improvement of the adhesion due to the microscale roughness or maybe to a relaxation of the osteogenesis constrain because the microroughness can enhance chondrogenesis.[34] Unfortunately, a deeper investigation using confocal reflection microscopy was not possible because of the high retention of the fluorescent probes used for the imaging by the nanostructured coating.

Cell morphology was assessed by SEM (Figure 3b). The surface roughness of the T2 substrates, with the addition of the insulating NPs and plasma polymers hindered a clear view of the cells that were more easily detected on T1 substrates (Supporting Information Figure S10). Cells were spread with a rounded shape in the samples with the carboxylic functionalization. On the other side, the not-treated and the amino-functionalized surfaces showed elongated structures with branching filipodia, which usually characterize osteoblasts. The highest degree of branching was observed on the T2 substrate with the nanostructured coating and electrophilic functionalization, thus showing the additional effect of nano- and microscale roughness to the chemistry guiding information.

The synergistic effect of chemistry and nanoroughness was even more evident observing the filipodia and the FA points (Supporting Information Figure S9). The filipodia were able to

DOI: 10.1021/acsami.8b15886
ACS Appl. Mater. Interfaces 2018, 10, 39512−39523

sense the roughness at the nanoscale.[16] Also, in the as-worked sample, the FA point originated from a surface defect of less than 100 nm and the filipodia has a similar size. As microroughness was added in T2 samples, the filipodia appeared thicker like ribbons about 350 nm wide, which stuck on higher and sharper asperities. As the NPs and a compliant surface chemistry were added, the filipodia fully laid on surfaces with the same size of the roughness' domes about 300 nm in diameter and were barely distinguishable from the coating.

However, the possibility to add surface functional groups and nanoroughness independently, with respect to standard commercial SBAE titanium substrates, enabled to further guide cell proliferation, leading, for example, to an improvement of 20% on cells adhesion.

3.3. Fibroblast Growth. In order to show the potentialities of the presented approach to reproduce chemistry and surface roughness on sensitive biopolymers, the same coatings deposited on titanium were deposited on PCL films (mp 60 °C, T_g −60 °C). In order to test their biological response, primary fibroblasts was selected as cells similar to osteoblasts but expected to be less sensitive to nanotopography.[24,38] No damage or change in surface morphology of the PCL film was observed after plasma polymer deposition.

In Figure 4a, the results of the in vitro tests are shown. Cell viability was evaluated at 24 h of culture measuring the metabolic activity by MTT test;[44] the samples with the nucleophilic functionalities showed similar behavior to untreated PCL, while the amine groups demonstrated a more than fivefold improvement. Electrophilic plasma polymers, in fact, present a similar chemistry with respect to the ester linkage of caprolactone, while in the literature, it is already known that amine groups enhance fibroblasts proliferation.[65] However, the effect of the NPs was particularly evident because they improved the viability of one order of magnitude with respect to PCL and of about a factor 2 with respect to a flat surface with the same chemistry.

Cell adhesion was evaluated following 15 min of culture. The results (Figure 4a) showed a dependence on both roughness and chemistry. In particular, the roughness allowed to improve the attachment of the cell to the surface even if with negative polarity: for both ammine and carboxylic functionalities, the nanotopography enhanced the adhesion of more than twofold, similar to viability results. This effect is due to the known capability of the filipodia to sense the surface at the nanoscale:[16] as they run into some nanotopographic features wide enough to allow the spatial clustering of 7−8 integrins, focal points can mature leading to cell adhesion to the surface.[18] Viability in this case is a consequence of the adhesion because the selected cells need a support for their survival.

A synergistic behavior of roughness and chemistry can be observed again for proliferation and p-FAK expression (Figure 4 and Supporting Information Figures S11 and S12). The surface chemistry with both polarities alone led to a small increase in the cell growth rate with respect to untreated PCL. As the roughness was added, cells replicated faster on the electrophilic surfaces, where the proliferation increased threefold and by a factor 10 compared to the not-coated PCL substrate. The addition of the nanoscale morphology, therefore, led always to remarkable improvements, and the effect is probably enhanced by the spherical shape of the

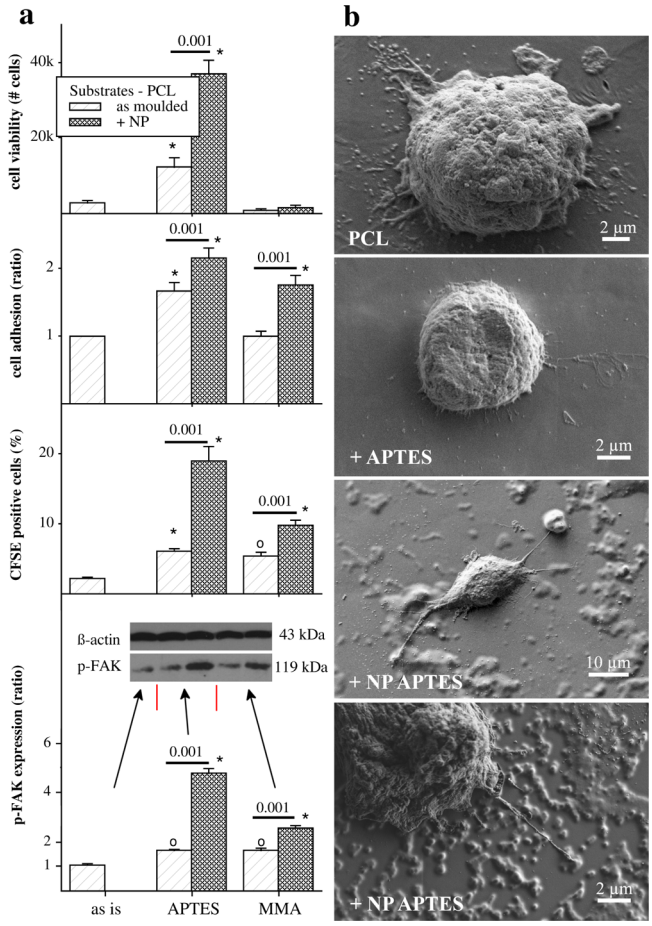

Figure 4. (a) Results of cell viability, cell adhesion (ratio vs as is), proliferation, and p-FAK expression (Western blot analysis and quantification, ratio vs as is)[66] for PCL films as is, with the plasma polymer coatings and with both plasma polymer and NPs (* 0.001 vs as is; ○ 0.01 vs as is) and (b) SEM images to highlight cells morphologies on PCL films as is, with the amine plasma polymer and with the NP and plasma polymer.

asperities that increases the mechanical stress in the FA points.[19] Mechanotransduction stimuli generate cytoskeletal tension and effects on the inner cell structure integrating assembly and disassembly of cytoskeletal filaments with transduction of nuclear imputes. Thus, roughness of supports promotes expression of proteins (i.e., YAP/TAZ; TWIST1) involved in long-time effects and able to modulate the NF-kB pathway for cell survival and proliferation.[67] It has to be considered that the PCL films have been moulded on atomically flat single crystal silicon wafers, where cells are not supported to find preferential anchoring for the maturation of the FA points. Then, the presence of the NPs is the only source of information for them on the surface apart from PCL chemistry. Conversely, the titanium substrates T1 and T2 were already presenting a certain roughness in the submicron range.

The morphology of the grown cells was observed by SEM (Figure 4b). Cells on the PCL film without the addition of nanostructures appeared in a rounded shape for all the surface chemical functionalities. On the surfaces with the amine groups, the filipodia seemed to protrude for longer distances as can be expected also by their higher adhesion. As the NPs were added in the deposited coating, the cells on the surface with carboxyl groups remained rounded, while with the amine

DOI: 10.1021/acsami.8b15886
ACS Appl. Mater. Interfaces 2018, 10, 39512−39523

groups, cells showed a strong elongation with the filipodia sensing the surface for distances comparable to cell size, seeking the nanoroughness for anchoring. It has to be highlighted that even if the NPs on the surface offer the cells micrometer scale defects, the FA point matures on the single NP edges. The dimension and density of the fixed NPs on the surface is therefore a key parameter that can be carefully controlled by the current deposition method.

On the two substrates for the two cell types considered, the surface chemistry and topography effect partially diverge. The results therefore highlight the importance to control the different parameters separately. Moreover, as pointed out in the introduction, in order to consider the synergistic effect of scaffold properties to guide cells growth, other parameters have to be considered such as, for example, scaffolds geometry and stiffness.

3.4. Fluorophore Release. Because the release of active molecules is a relevant topic in medical implants, we have investigated the potential use of the NPs as release agents. NPs can be considered, indeed, not only as building blocks for the nanoscale roughness construction, but also as smart carriers. Inorganic materials for calcium or strontium ions release can substitute the silica nanospheres with no critical risk for process implementation. However, the low temperature of the process allows for even higher flexibility; for example, biodegradable polymer particles can be used and if a bioactive molecule was previously embedded, then it is released, while the polymer dissolves in the body fluids.[68] Because the plasma process does not alter the biopolymer, no change in the active molecule can be expected. In order to verify this statement, we have considered a fluorescent dye as model drug embedded in a bioresorbable polymer. Therefore, PLGA Degradex particles, with an average diameter of 200 nm and with an embedded red fluorophore, were fixed on silicon and titanium T1 surfaces by a plasma polymer starting from an MMA precursor. For particle spraying, three different dispersions in ethanol were prepared mixing PLGA Degradex with silica NPs in three different concentrations (1, 10, and 100%).

The deposited coating on the silicon substrate can be observed in Figure 5d. The size distribution of the PLGA NPs was quite wide and goes from micrometer agglomerates (Supporting Information Figure S13) that could not be fixed on the surface by the 150 nm thick coating, up to submicrometers or tens of nanometers in diameter. The coating appeared always with the same morphology with void defects close to the particles due to the self-shadowing effect. In the cross section (Figure 5e), a PLGA particle can be distinguished below the coating, demonstrating that it was not damaged or melted during the plasma process.

The coated T1 substrate was used for the pre-osteoblastic murine cell line culture for 5 days, and then it was washed. The PLGA NPs are characterized by a two-step mechanism of release of the active molecules: a burst release that is related to random scission of the polymer chains followed by diffusion and a slower process due to polymer dissolution. Therefore, for both mechanisms, the smaller is the particle faster is the delivery. For the few hundreds nanometre size, a burst release can be expected within the first 100 h.[69] In order to verify the release, in our case, the fluorophore was quantified in the culture media for the three different concentrations. The results, presented in Figure 5a, did not scale exactly as a function of the PLGA particle concentration. This behavior was probably due to the presence of microaggregates, which

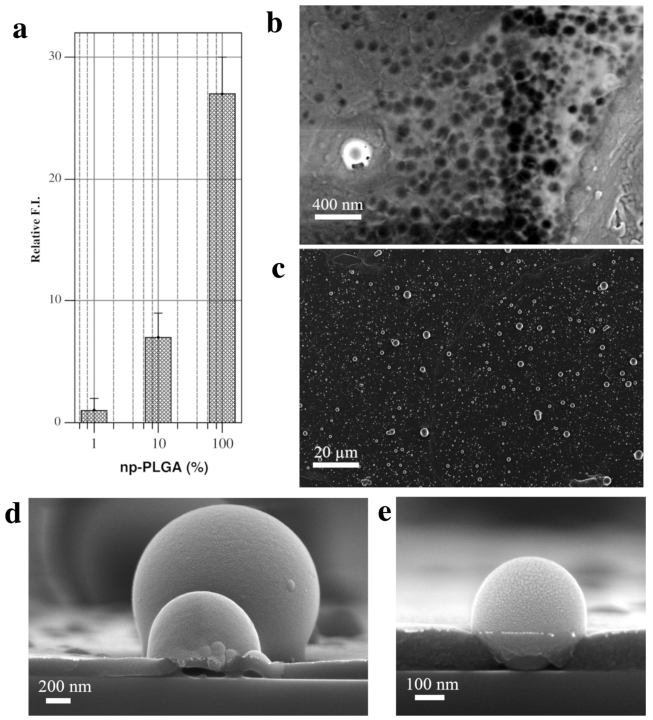

Figure 5. (a) Relative fluorescence intensity in the solution after 5 days of osteoblasts culture spraying by aerosol the silica and PLGA NPs in the same dispersion at different concentrations; (b,c) SEM images of the T1 surfaces with 100% PLGA particles fixed with an MMA layer, before (c) and after (b) the cells culture. (d,e) SEM cross sections of the coating with the PLGA particles which highlighted the presence of the particles under the domes (e) and the voids in the fixing coating due to particle shadowing (d).

were most likely at higher concentrations and could not be fixed on the surface efficiently. The expected trend and fluorophore integrity were maintained, demonstrating the protective role of the polymer.

The surface of the sample was observed by SEM before and after cell culture. In Figure 5b,c, the images relative to the sample with PLGA concentration of 100% are presented. In the top view of the as-deposited surface (Figure 5c), the macroaggregates of several micrometres as well as the smaller particles randomly distributed are clearly visible. After cell culture (Figure 5b), the particles were dissolved in the fluids and on voids in the coating remained on the surface of the T1 substrates. In the image 5b, an isolated NP with still the top coating can be observed, at the same time presenting some opening in correspondence with the void defects around the particle. The image therefore suggests that those voids are the preferential communication path between the embedded NPs and the culture media. Their closing by increasing the coating thickness could therefore allow for a permeability control, slowing down the delivery of the active molecules.

4. CONCLUSIONS

A process to deposit a nanostructured coating is here presented and validated as proof of concept, demonstrating the possibility to design the surface feature of scaffolds and implants by dealing separately with nanoscale roughness, surface chemistry, and delivery of active agents.

The procedure consists of two steps: an aerosol deposition of a NPs dispersion, followed by a plasma polymer coating

DOI: 10.1021/acsami.8b15886
ACS Appl. Mater. Interfaces 2018, 10, 39512−39523

using an APPJ. The deposition of the NPs was used to control the nanoscale morphology on flat and microrough surfaces: size and density of the NP deposited can be used to tune spatial and vertical roughness. The APPJ deposits a stable fixing layer that envelops the particles and at the same time offers the desired surface functionalities, depending on the chosen precursor. The fixing coating presented a void defect around the particle, which can be used as the preferential path for the release of active agents if nanocarriers are used to create the roughness.

The proposed approach was tested in vitro with the preosteoblast murine cells line on titanium substrates for potential applications as dental implants and with skin fibroblasts on PCL for tissue regeneration scaffolds. On titanium substrates, it was possible to highlight the synergistic effect of chemistry and morphology in enhancing the selectivity of the differentiation process. In particular, cell proliferation was enhanced of about the 20% even compared to the SBAE substrate. Also, on the PCL substrates, the nanostructures improved fibroblast adhesion. The possibility to control morphology and chemistry separately on PCL allowed to highlight their synergistic effect with elongated cells seeking the NPs for the FA maturation on amino functionalities. This synergistic effect enhanced fibroblast proliferation by a factor 10 compared to the smooth PCL substrate. In the end, bioresorbable fluorescent NPs were used to create the roughness, and the release of their undamaged red fluorophore in the cell culture media was checked.

The nanostructured coating deposition is performed at temperatures lower than 50 °C; it allows for the treatment of sensitive material, such as biopolymers, but also similarly on a variety of substrates including metallic, polymeric, insulating or conductive.

The technology can be further developed, for example, by the introduction in the resorbable NPs active molecules such as growth factors or antibiotics or by the implementation of conductive coatings deposited by APPJ. From the technological point of view, the deposition process proposed here is based on spraying technologies at an equivalent rate of 0.5 $mm{\cdot}s^{-1}$, which is compatible with the speed range of the extrusion printing technologies ($0.01-150\ mm{\cdot}s^{-1}$).[70] Our approach can therefore be potentially implemented on 3D systems in order to obtain a localized control of roughness, surface chemistry, and drug release.

■ ASSOCIATED CONTENT

Supporting Information

The Supporting Information is available free of charge on the ACS Publications website at DOI: 10.1021/acsami.8b15886.

SI_Nanobio.pdf: AFM of the untreated substrates, APPJ scheme and description, plasma process temperature and electrical characterization, silica NP SEM, and size distribution, plasma process parameters for the coatings deposition, cross-sectional SEM images of the nanostructured coating, AFM surface morphologies of the nanostructured coatings, SEM images of the filipodia on the different substrates, cell morphology by SEM images on T1 substrates, fibroblast proliferation assays, and size distribution of PLGA Degradex particles (PDF)

■ AUTHOR INFORMATION

Corresponding Author

*E-mail: alessandro.patelli@unipd.it. Phone: +39 049 827 7039.

ORCID

Alessandro Patelli: 0000-0001-7662-4352
Federico Mussano: 0000-0001-5800-0749
Emmanuele Ambrosi: 0000-0002-1834-6144
Niccoló Michieli: 0000-0002-9357-7380
Paolo Scopece: 0000-0003-1466-5823
Lorenzo Moroni: 0000-0003-1298-6025

Notes

The authors declare no competing financial interest.

■ ACKNOWLEDGMENTS

The authors A.P., P.S., and L.M. are grateful to European Union's Horizon 2020 research and innovation programme, LEIT Advanced Manufacturing and Processing action, under grant agreement no. 685825, project "FAST". All the data needed to evaluate the conclusions made in this paper are present within the data presented in the paper and/or the Supporting Information. Additional data may be requested from the authors.

■ REFERENCES

(1) Yu, X.; Tang, X.; Gohil, S. V.; Laurencin, C. T. Biomaterials for Bone Regenerative Engineering. *Adv. Healthcare Mater.* **2015**, *4*, 1268−1285.

(2) Li, Y.; Xiao, Y.; Liu, C. The Horizon of Materiobiology: A Perspective on Material-Guided Cell Behaviors and Tissue Engineering. *Chem. Rev.* **2017**, *117*, 4376−4421.

(3) Di Luca, A.; Lorenzo-Moldero, I.; Mota, C.; Lepedda, A.; Auhl, D.; Van Blitterswijk, C.; Moroni, L. Tuning Cell Differentiation into a 3D Scaffold Presenting a Pore Shape Gradient for Osteochondral Regeneration. *Adv. Healthcare Mater.* **2016**, *5*, 1753−1763.

(4) Arima, Y.; Iwata, H. Effect of Wettability and Surface Functional Groups on Protein Adsorption and Cell Adhesion Using Well-Defined Mixed Self-Assembled Monolayers. *Biomaterials* **2007**, *28*, 3074−3082.

(5) Santos, P. A.; Rocha, C. S.; Baptista, M. S. Adhesion and Proliferation of HeLa and Fibroblast Cells on Chemically-Modified Gold Surfaces. *Colloids Surf., B* **2014**, *123*, 429−438.

(6) Agarwal, R.; García, A. J. Biomaterial Strategies for Engineering Implants for Enhanced Osseointegration and Bone Repair. *Adv. Drug Delivery Rev.* **2015**, *94*, 53−62.

(7) Cools, P.; Ghobeira, R.; Van Vrekhem, S.; De Geyterand, N.; Morent, R. *Plasma Science and Technology—Progress in Physical States and Chemical Reactions*; InTech, 2016; Chapter 8, pp 201−240.

(8) Surucu, S.; Masur, K.; Turkoglu Sasmazel, H.; Von Woedtke, T.; Weltmann, K. D. Atmospheric Plasma Surface Modifications of Electrospun PCL/Chitosan/PCL Hybrid Scaffolds by Nozzle Type Plasma Jets for Usage of Cell Cultivation. *Appl. Surf. Sci.* **2016**, *385*, 400−409.

(9) Schröder, K.; Finke, B.; Ohl, A.; Lüthen, F.; Bergemann, C.; Nebe, B.; Rychly, J.; Walschus, U.; Schlosser, M.; Liefeith, K.; Neumann, H.-G.; Weltmann, K.-D.; Taylor, P. Capability of Differently Charged Plasma Polymer Coatings for Control of Tissue Interactions with Titanium Surfaces. *J. Adhes. Sci. Technol.* **2010**, *24*, 1191−1205.

(10) Mussano, F.; Genova, T.; Verga Falzacappa, E.; Scopece, P.; Munaron, L.; Rivolo, P.; Mandracci, P.; Benedetti, A.; Carossa, S.; Patelli, A. In vitro characterization of two different atmospheric plasma jet chemical functionalizations of titanium surfaces. *Appl. Surf. Sci.* **2017**, *409*, 314−324.

DOI: 10.1021/acsami.8b15886
ACS Appl. Mater. Interfaces 2018, 10, 39512−39523

(11) Griffin, M. F.; Ibrahim, A.; Seifalian, A. M.; Butler, P. E. M.; Kalaskar, D. M.; Ferretti, P. Chemical Group-Dependent Plasma Polymerisation Preferentially Directs Adipose Stem Cell Differentiation Towards Osteogenic or Chondrogenic Lineages. *Acta Biomater.* **2017**, *50*, 450−461.
(12) Intranuovo, F.; Gristina, R.; Brun, F.; Mohammadi, S.; Ceccone, G.; Sardella, E.; Rossi, F.; Tromba, G.; Favia, P. Plasma Modification of PCL Porous Scaffolds Fabricated by Solvent-Casting/Particulate-Leaching for Tissue Engineering. *Plasma Processes Polym.* **2014**, *11*, 184−195.
(13) Curran, J. M.; Chen, R.; Hunt, J. A. The Guidance of Human Mesenchymal Stem Cell Differentiation In Vitro by Controlled Modifications to the Cell Substrate. *Biomaterials* **2006**, *27*, 4783−4793.
(14) Goddard, J. M.; Hotchkiss, J. H. Polymer Surface Modification for the Attachment of Bioactive Compounds. *Prog. Polym. Sci.* **2007**, *32*, 698−725.
(15) Watari, S.; Hayashi, K.; Wood, J. A.; Russell, P.; Nealey, P. F.; Murphy, C. J.; Genetos, D. C. Modulation of Osteogenic Differentiation in hMSCs Cells by Submicron Topographically-Patterned Ridges and Grooves. *Biomaterials* **2012**, *33*, 128−136.
(16) Dalby, M.; Riehle, M. O.; Johnstone, H.; Affrossman, S.; Curtis, A. S. Investigating the Limits of Filopodial Sensing: A Brief Report using SEM to Image the Interaction Between 10 nm High Nano-Topography and Fibroblast Filopodia. *Cell Biol. Int.* **2004**, *28*, 229−236.
(17) Dalby, M. J.; Gadegaard, N.; Oreffo, R. O. C. Harnessing nanotopography and integrin-matrix interactions to influence stem cell fate. *Nat. Mater.* **2014**, *13*, 558−569.
(18) Cavalcanti-Adam, E. A.; Spatz, J. P. Receptor Clustering Control and Associated Force Sensing by Surface Patterning: When Force Matters. *Nanomedicine* **2015**, *10*, 681−684.
(19) Di Cio, S.; Gautrot, J. E. Cell Sensing of Physical Properties at the Nanoscale: Mechanisms and Control of Cell Adhesion and Phenotype. *Acta Biomater.* **2016**, *30*, 26−48.
(20) Shen, X.; Ma, P.; Hu, Y.; Xu, G.; Zhou, J.; Cai, K. Mesenchymal Stem Cell Growth Behavior on Micro/Nano Hierarchical Surfaces of Titanium Substrates. *Colloids Surf., B* **2015**, *127*, 221−232.
(21) Gittens, R. A.; McLachlan, T.; Olivares-Navarrete, R.; Cai, Y.; Berner, S.; Tannenbaum, R.; Schwartz, Z.; Sandhage, K. H.; Boyan, B. D. The Effects of Combined Micron-/Submicron-Scale Surface Roughness and Nanoscale Features on Cell Proliferation and Differentiation. *Biomaterials* **2011**, *32*, 3395−3403.
(22) Zhao, L.; Mei, S.; Chu, P. K.; Zhang, Y.; Wu, Z. The Influence of Hierarchical Hybrid Micro/Nano-Textured Titanium Surface with Titania Nanotubes on Osteoblast Functions. *Biomaterials* **2010**, *31*, 5072−5082.
(23) Limongi, T.; Tirinato, L.; Pagliari, F.; Giugni, A.; Allione, M.; Perozziello, G.; Candeloro, P.; Di Fabrizio, E. Fabrication and Applications of Micro/Nanostructured Devices for Tissue Engineering. *Nano-Micro Lett.* **2017**, *9*, 1.
(24) Mendonça, G.; Mendonça, D. B. S.; Aragão, F. J. L.; Cooper, L. F. Advancing Dental Implant Surface Technology - From Micron- to Nanotopography. *Biomaterials* **2008**, *29*, 3822−3835.
(25) Kumar, G.; Waters, M. S.; Farooque, T. M.; Young, M. F.; Simon, C. G. Freeform Fabricated Scaffolds with Roughened Struts that Enhance Both Stem Cell Proliferation and Differentiation by Controlling Cell Shape. *Biomaterials* **2012**, *33*, 4022−4030.
(26) Gunnewiek, M. K.; Di Luca, A.; Bollemaat, H. Z.; van Blitterswijk, C. A.; Vancso, G. J.; Moroni, L.; Benetti, E. M. Creeping Proteins in Microporous Structures: Polymer Brush-Assisted Fabrication of 3D Gradients for Tissue Engineering. *Adv. Healthcare Mater.* **2015**, *4*, 1169−1174.
(27) Raphel, J.; Holodniy, M.; Goodman, S. B.; Heilshorn, S. C. Multifunctional Coatings to Simultaneously Promote Osseointegration and Prevent Infection of Orthopaedic Implants. *Biomaterials* **2016**, *84*, 301−314.
(28) Zhang, W.; Wang, G.; Liu, Y.; Zhao, X.; Zou, D.; Zhu, C.; Jin, Y.; Huang, Q.; Sun, J.; Liu, X.; Jiang, X.; Zreiqat, H. The Synergistic Effect of Hierarchical Micro/Nano-Topography and Bioactive Ions for Enhanced Osseointegration. *Biomaterials* **2013**, *34*, 3184−3195.
(29) Meng, Y.; Li, X.; Li, Z.; Liu, C.; Zhao, J.; Wang, J.; Liu, Y.; Yuan, X.; Cui, Z.; Yang, X. Surface Functionalization of Titanium Alloy with miR-29b Nanocapsules to Enhance Bone Regeneration. *ACS Appl. Mater. Interfaces* **2016**, *8*, 5783−5793.
(30) Sears, N. A.; Seshadri, D. R.; Dhavalikar, P. S.; Cosgriff-Hernandez, E. A Review of Three-Dimensional Printing in Tissue Engineering. *Tissue Eng., Part B* **2016**, *22*, 298−310.
(31) Qazi, T. H.; Mooney, D. J.; Pumberger, M.; Geißler, S.; Duda, G. N. Biomaterials Based Strategies for Skeletal Muscle Tissue Engineering: Existing Technologies and Future Trends. *Biomaterials* **2015**, *53*, 502−521.
(32) Murphy, S. V.; Atala, A. 3D bioprinting of tissues and organs. *Nat. Biotechnol.* **2014**, *32*, 773−785.
(33) Goldman, M.; Juodzbalys, G.; Vilkinis, V. Titanium Surfaces with Nanostructures Influence on Osteoblasts Proliferation: a Systematic Review. *J. Oral Maxillofac. Res.* **2014**, *5*, No. e1.
(34) Neves, S. C.; Mota, C.; Longoni, A.; Barrias, C. C.; Granja, P. L.; Moroni, L. Additive Manufactured Polymeric 3D Scaffolds with Tailored Surface Topography Influence Mesenchymal Stromal Cells Activity. *Biofabrication* **2016**, *8*, 025012.
(35) Zhu, W.; Webster, T. J.; Zhang, L. G. How Can 3D Printing Be a Powerful Tool in Nanomedicine? *Nanomedicine* **2018**, *13*, 251−253.
(36) Domingos, M.; Intranuovo, F.; Gloria, A.; Gristina, R.; Ambrosio, L.; Bártolo, P. J.; Favia, P. Improved Osteoblast Cell Affinity on Plasma-Modified 3-D Extruded PCL Scaffolds. *Acta Biomater.* **2013**, *9*, 5997−6005.
(37) Wang, M.; Favi, P.; Cheng, X.; Golshan, N. H.; Ziemer, K. S.; Keidar, M.; Webster, T. J. Cold Atmospheric Plasma (CAP) Surface Nanomodified 3D Printed Polylactic Acid (PLA) Scaffolds for Bone Regeneration. *Acta Biomater.* **2016**, *46*, 256−265.
(38) Webster, T. J.; Ergun, C.; Doremus, R. H.; Siegel, R. W.; Bizios, R. Specific Proteins Mediate Enhanced Osteoblast Adhesion on Nanophase Ceramics. *J. Biomed. Mater. Res.* **2000**, *51*, 475−483.
(39) Lo Porto, C.; Palumbo, F.; Buxadera-Palomero, J.; Canal, C.; Jelinek, P.; Zajickova, L.; Favia, P. On the Plasma Deposition of Vancomycin-Containing Nano-Capsules for Drug-Delivery Applications. *Plasma Processes Polym.* **2018**, *15*, 1700232.
(40) (a) Patelli, A.; Verga Falzacappa, E.; Scopece, P.; Pierobon, R.; Vezzù, S. Method for Generating an Atmospheric Plasma Jet and Atmospheric Plasma Minitorch Device. U.S. Patent 9,693,441 B2, 2015. (b) Patelli, A.; Verga, E.; Nodari, L.; Petrillo, S. M.; Delva, A.; Ugo, P.; Scopece, P. A Customised Atmospheric Pressure Plasma Jet for Conservation Requirements. *IOP Conf. Ser. Mater. Sci. Eng.* **2018**, *364*, 012079.
(41) Simon, D.; Holland, A.; Shanks, R. Poly(caprolactone) Thin Film Preparation, Morphology, and Surface Texture. *J. Appl. Polym. Sci.* **2007**, *103*, 1287−1294.
(42) Costacurta, S.; Falcaro, P.; Vezzù, S.; Colasuonno, M.; Scopece, P.; Zanchetta, E.; Guglielmi, M.; Patelli, A. Fabrication of functional nanostructured coatings by a combined sol-gel and plasma-enhanced chemical vapour deposition method. *J. Sol-Gel Sci. Technol.* **2011**, *60*, 340−346.
(43) Mardegan, A.; Pifferi, V.; Pontoglio, E.; Falciola, L.; Scopece, P.; Moretto, L. M. Sprayed Carbon Nanotubes on Pyrolysed Photoresist Carbon Electrodes: Application to O-Toluidine Determination. *Electrochem. Commun.* **2014**, *48*, 13−16.
(44) Stockert, J. C.; Blázquez-Castro, A.; Cañete, M.; Horobin, R. W.; Villanueva, Á. MTT Assay for Cell Viability: Intracellular Localization of the Formazan Product is in Lipid Droplets. *Acta Histochem.* **2012**, *114*, 785−796.
(45) Shen, X.; Ho, C.-M.; Wong, T.-S. Minimal Size of Coffee Ring Structure. *J. Phys. Chem. B* **2010**, *114*, 5269−5274.
(46) (a) Foest, R.; Kindel, E.; Lange, H.; Ohl, A.; Stieber, M.; Weltmann, K.-D. RF Capillary Jet - a Tool for Localized Surface Treatment. *Contrib. Plasma Phys.* **2007**, *47*, 119−128. (b) DIN EN 60601-1-6:2010: Medical electrical equipment (IEC 60601-1-6:2010), 2015.

DOI: 10.1021/acsami.8b15886
ACS Appl. Mater. Interfaces 2018, 10, 39512−39523

(47) Xaubet, M.; Baudler, J.-S.; Gerling, T.; Giuliani, L.; Minotti, F.; Grondona, D.; Von Woedtke, T.; Weltmann, K.-D. Design Optimization of an Air Atmospheric Pressure Plasma-Jet Device Intended for Medical Use. *Plasma Processes Polym.* **2018**, *15*, 1700211.
(48) Friedrich, J. Mechanisms of Plasma Polymerization - Reviewed from a Chemical Point of View. *Plasma Processes Polym.* **2011**, *8*, 783−802.
(49) Finke, B.; Rebl, H.; Hempel, F.; Schäfer, J.; Liefeith, K.; Weltmann, K.-D.; Nebe, J. B. Aging of Plasma-Polymerized Allylamine Nanofilms and the Maintenance of Their Cell Adhesion Capacity. *Langmuir* **2014**, *30*, 13914−13924.
(50) Vinogradov, I.; Zimmer, D.; Lunk, A. Diagnostics of SiCOH-Film-Deposition in the Dielectric Barrier Discharge at Atmospheric Pressure. *Plasma Processes Polym.* **2007**, *4*, S435−S439.
(51) Gengenbach, T. R.; Griesser, H. J. Deposition Conditions Influence the Postdeposition Oxidation of Methyl Methacrylate Plasma Polymer Films. *J. Polym. Sci., Part A: Polym. Chem.* **1998**, *36*, 985−1000.
(52) Liguori, A.; Pollicino, A.; Stancampiano, A.; Tarterini, F.; Focarete, M. L.; Colombo, V.; Gherardi, M. Deposition of Plasma-Polymerized Polyacrylic Acid Coatings by a Non-Equilibrium Atmospheric Pressure Nanopulsed Plasma Jet. *Plasma Processes Polym.* **2016**, *13*, 375−386.
(53) Pan, Y. V.; Barrios, E. Z.; Denton, D. D. In situ FTIR investigation of MMA plasmas, plasma-polymerized films, and reaction mechanisms. *J. Polym. Sci., Part A: Polym. Chem.* **1998**, *36*, 587−602.
(54) Sano, S.; Kato, K.; Ikada, Y. Introduction of functional groups onto the surface of polyethylene for protein immobilization. *Biomaterials* **1993**, *14*, 817−822.
(55) Barabasi, A.-L.; Stanley, H. E. *Fractal Concepts in Surface Growth*; Press Syndacate of the University of Cambridge: Cambridge, 1995; Chapter 5, p 388.
(56) Meakin, P.; Jullien, R. Restructuring Effects in the Rain Model for Random Deposition. *J. Phys.* **1987**, *48*, 1651−1662.
(57) Jullien, R.; Meakin, P. Simple Three-Dimensional Models for Ballistic Deposition with Restructuring. *Europhys. Lett.* **1987**, *4*, 1385−1390.
(58) Meakin, P. Historical Introduction to Computer Models for Fractal Aggregates. *J. Sol-Gel Sci. Technol.* **1999**, *15*, 97−117.
(59) Kubisztal, J.; Kubisztal, M.; Haneczok, G. Quantitative characterization of material surface - Application to Ni + Mo electrolytic composite coatings. *Mater. Charact.* **2016**, *122*, 45−53.
(60) Tolman, S.; Meakin, P. Off-lattice and hypercubic-lattice models for diffusion-limited aggregation in dimensionalities 2-8. *Phys. Rev. A: At., Mol., Opt. Phys.* **1989**, *40*, 428−437.
(61) Ferré-Borrull, J.; Duparré, A.; Quesnel, E. Procedure to Characterize Microroughness of Optical Thin Films: Application to Ion-Beam-Sputtered Vacuum-Ultraviolet Coatings. *Appl. Opt.* **2001**, *40*, 2190.
(62) Genova, T.; Munaron, L.; Carossa, S.; Mussano, F. Overcoming physical constraints in bone engineering: 'the importance of being vascularized'. *J. Biomater. Appl.* **2016**, *30*, 940−951.
(63) Canullo, L.; Genova, T.; Naenni, N.; Nakajima, Y.; Masuda, K.; Mussano, F. Plasma of Argon Enhances the Adhesion of Murine Osteoblasts on Different Graft Materials. *Ann. Anat.* **2018**, *218*, 265−270.
(64) Xie, X.; Mao, C.; Liu, X.; Tan, L.; Cui, Z.; Yang, X.; Zhu, S.; Li, Z.; Yuan, X.; Zheng, Y.; Yeung, K. W. K.; Chu, P. K.; Wu, S. Tuning the Bandgap of Photo-Sensitive Polydopamine/Ag3PO4/Graphene Oxide Coating for Rapid, Noninvasive Disinfection of Implants. *ACS Cent. Sci.* **2018**, *4*, 724−738.
(65) Altankov, G.; Richau, K.; Groth, T. The Role of Surface Zeta Potential and Substratum Chemistry for Regulation of Dermal Fibroblasts Interaction. *Mater. Werkst.* **2003**, *34*, 1120−1128.
(66) Mao, C.; Xiang, Y.; Liu, X.; Cui, Z.; Yang, X.; Li, Z.; Zhu, S.; Zheng, Y.; Yeung, K. W. K.; Wu, S. Repeatable Photodynamic Therapy with Triggered Signaling Pathways of Fibroblast Cell Proliferation and Differentiation To Promote Bacteria-Accompanied Wound Healing. *ACS Nano* **2018**, *12*, 1747−1759.
(67) Wang, N. Review of Cellular Mechanotransduction. *J. Phys. D: Appl. Phys.* **2017**, *50*, 233002.
(68) Makadia, H. K.; Siegel, S. J. Poly Lactic-co-Glycolic Acid (PLGA) as Biodegradable Controlled Drug Delivery Carrier. *Polymers* **2011**, *3*, 1377−1397.
(69) Ortega-Oller, I.; Padial-Molina, M.; Galindo-Moreno, P.; O'Valle, F.; Jódar-Reyes, A. B.; Peula-García, J. M. Bone Regeneration from PLGA Micro-Nanoparticles. *BioMed Res. Int.* **2015**, *2015*, 1−18.
(70) Zhu, W.; Ma, X.; Gou, M.; Mei, D.; Zhang, K.; Chen, S. 3D Printing of Functional Biomaterials for Tissue Engineering. *Curr. Opin. Biotechnol.* **2016**, *40*, 103−112.

DOI: 10.1021/acsami.8b15886
ACS Appl. Mater. Interfaces 2018, 10, 39512−39523